

The Quantum Anomalous Hall Majorana Platform

Yongxin Zeng,¹ Chao Lei,² Gaurav Chaudhary,² and Allan H. MacDonald²

¹CAS Key Laboratory of Strongly-Coupled Quantum Matter Physics, and Department of Physics, University of Science and Technology of China, Hefei, Anhui 230026, China.

²Department of Physics, The University of Texas at Austin, Austin, Texas 78712, USA
(Dated: July 21, 2022)

We show that quasi-one-dimensional (1D) quantum wires can be written onto the surface of magnetic topological insulator (MTI) thin films by gate arrays. When the MTI is in a quantum anomalous Hall (QAH) state, MTI/superconductor (SC) quantum wires have especially broad stability regions for both topological and non-topological states, facilitating creation and manipulation of Majorana particles on the MTI surface.

PACS numbers: 71.70.Ej, 71.10.Pm, 74.45.+c,

Introduction: Non-Abelian anyons that can be localized at controllable positions provide an attractive platform for fault-tolerant quantum computation [1–7]. Candidate non-Abelian particles that have already been realized in solid state systems include fractionally charged excitations of the $\nu = 5/2$ fractional quantum Hall liquid [8], Abrikosov vortices in two-dimensional topological superconductors [9], and Majorana zero mode (MZM) end states of p -wave superconducting quantum wires [10–13]. In this article we propose a new strategy for creation of MZMs and manipulations of MZM positions on a two-dimensional surface.

MZMs appear at boundaries between normal and topological quasi-1D superconductors [10, 12–14]. The simplest 1D topological superconductor (TSC) consists of spinless electrons with near-neighbor attractive interactions [10]. Topological superconducting states can occur, however, in any quasi-1D system with superconductivity and broken time-reversal symmetry [11]. Much progress has been achieved both theoretically [12, 13, 15] and experimentally [16–21] by studying strongly spin-orbit-coupled proximitized quantum wires with large g -factors that are perturbed by an external magnetic field, and also by placing magnetic-atom arrays on superconducting substrates [22, 23]. Here we suggest an alternate approach, based on the QAH state [24–26] of MTIs, that has potentially valuable advantages. We show that ribbons formed from MTIs are often topological when proximity-coupled to a superconductor. MZMs also appear when quasi-1D topological regions are written onto a portion of the surface of an MTI by external gates, as illustrated schematically in Fig. 1. Furthermore, the MTI/SC phase diagram has particularly broad regions of stability for both normal and topological phases when the isolated MTI is close to a phase boundary between normal insulator and QAH states [24, 25]. This property provides a practical route towards electrical control of Majorana positions, and braiding operations via Majorana T-junctions [27], and recently proposed Majorana box qubit [7, 28].

Theoretical model of a proximized MTI: We focus on Cr-

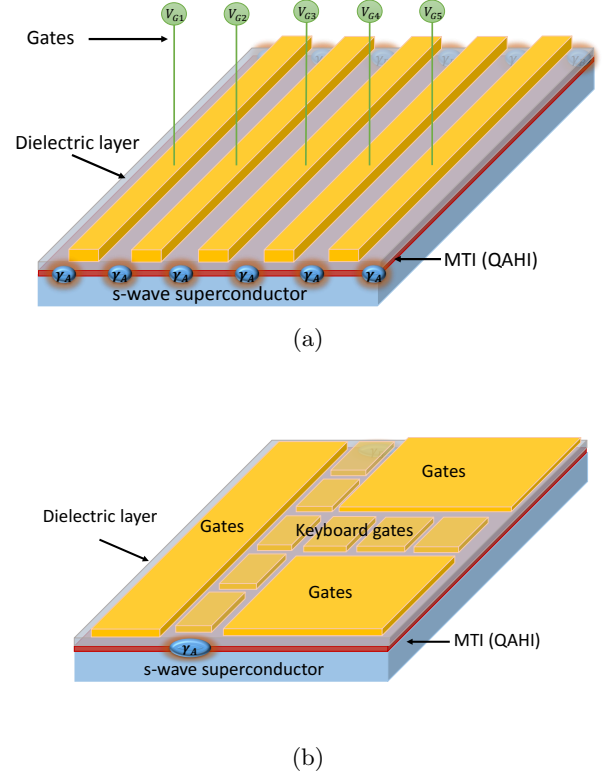


FIG. 1: (a) Majorana zero modes can be created locally by separating the surface of a magnetic topological insulator in a Quantum Anomalous Hall state into alternating normal and topological regions using remote gates; (b) A T-junction can be defined and controlled by local gates to achieve manipulation and braiding of Majoranas.

doped Bi_2Se_3 thin films in which proximitized superconductivity has already been demonstrated [25, 26] experimentally, and which are close to the MTI's QAH insulator/normal insulator phase boundary when 4-6 quintile layers thick. In the $\phi_{\mathbf{k}} = (c_{\mathbf{k}\uparrow}^t, c_{\mathbf{k}\downarrow}^t, c_{\mathbf{k}\uparrow}^b, c_{\mathbf{k}\downarrow}^b)^T$ basis, where $c_{\mathbf{k}\sigma}^s$ annihilates an electron with momentum \mathbf{k} , spin $\sigma = \uparrow, \downarrow$ and surface $s = t/b$ (top/bottom), the single par-

ticle Hamiltonian of a MTI thin film at energies below the bulk gap is

$$H_0(\mathbf{k}) = h_D(\mathbf{k})\tau_z + m_k\tau_x + \lambda\sigma_z + \lambda'\tau_z \quad (1)$$

where τ_i acts on surface and σ_i on spin. In Eq. 1 $h_D(\mathbf{k}) = v(k_y\sigma_x - k_x\sigma_y)$ is the 2D Dirac isolated surface Hamiltonian with Fermi velocity v ; $m_k = m_0 + m_1(k_x^2 + k_y^2)$ accounts for hybridization between top and bottom surfaces, λ is the exchange field produced by the ferromagnetically ordered magnetic dopants; and λ' accounts for the energetic displacement between Dirac cones on top and bottom surfaces produced by vertical electric fields in the bulk of the TI. When placed in proximity to an s -wave SC, the system is described by the Bogoliubov-de Gennes (BdG) Hamiltonian $H(\mathbf{k}) = \sum_{\mathbf{k}} \psi_{\mathbf{k}}^\dagger H_{\text{BdG}}(\mathbf{k}) \psi_{\mathbf{k}}/2$, where

$$H_{\text{BdG}}(\mathbf{k}) = \begin{pmatrix} H_0(\mathbf{k}) - \mu & \Delta_{\text{sc}} \\ \Delta_{\text{sc}}^\dagger & -H_0^*(-\mathbf{k}) + \mu \end{pmatrix} \quad (2)$$

with

$$\Delta_{\text{sc}} = \begin{pmatrix} i\Delta_t\sigma_y & 0 \\ 0 & i\Delta_b\sigma_y \end{pmatrix}. \quad (3)$$

and

$$\psi_{\mathbf{k}} = (c_{\mathbf{k}\uparrow}^t, c_{\mathbf{k}\downarrow}^t, c_{\mathbf{k}\uparrow}^b, c_{\mathbf{k}\downarrow}^b, c_{-\mathbf{k}\uparrow}^{t\dagger}, c_{-\mathbf{k}\downarrow}^{t\dagger}, c_{-\mathbf{k}\uparrow}^{b\dagger}, c_{-\mathbf{k}\downarrow}^{b\dagger})^T \quad (4)$$

A regularized square-lattice version of Eq. 2 with nearest neighbor hopping [29] accurately and conveniently captures the physics of topological phase transitions (TPT) at the surface of MTI. In the lattice model $k_{x/y}$ is replaced by $\sin k_{x/y}$ and k^2 by $2(2 - \cos k_x - \cos k_y)$. We absorb the lattice constant into the wavevectors in Eq. 1 to make them dimensionless, so that m_0, m_1 and v all have dimensions of energy. The inter-surface hybridization parameter m_1 plays an essential role by preventing the appearance of unphysical states at low energies away from $\mathbf{k} = 0$. For $m_0 \ll m_1$ only the Γ -point avoided crossing is relevant at low energies. We can obtain realistic values of v , m_0 and m_1 by comparing the model spectrum with DFT band structures of Bi_2Se_3 , like the one illustrated Fig. S1 of the Supplemental Material. For a five-layer film we find that the gap at Γ is about 12 meV, giving $m_0 = 6$ meV. Rough estimates for m_1 and v can be obtained by fitting to the DFT Dirac velocity v ($\sim 4 \times 10^5$ m/s) and the DFT gaps at M and K . We find that $m_1 \sim 0.2$ eV and $v \sim 0.7$ eV (notice that the lower band of DFT result gives a different value of v). As shown in the Supplemental Material, our main findings on topological robustness are independent of upper or lower band Fermi velocity as long as v and m_1 remains on larger energy scale compared to m_0) for a lattice model with lattice constant $a \approx 4\text{\AA}$.

Topological classification of 2D bulk and 1D ribbon states: The 2D classification of MTI/SC states presented in

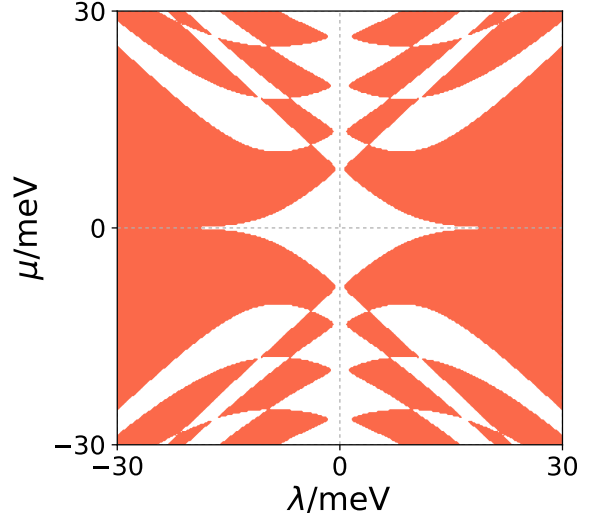


FIG. 2: Z_2 ribbon phase diagram in (λ, μ) space for $\lambda' = 0$, $m_0 = 6$ meV, $m_1 = 200$ meV, $\Delta_b = 1$ meV, $\Delta_t = 0$, ribbon width $W = 300$, and velocity $v = 700$ meV. The orange regions are topologically non-trivial and support MZMs.

Ref. 30 demonstrates the possibility of BdG bands with odd Chern numbers. We first address the special case $\Delta_t = -\Delta_b = \Delta$ and set $\lambda' = \mu = 0$ to obtain simple analytical expressions for phase boundaries. When the basis transformation used in Ref. 30 is employed the 8×8 BdG Hamiltonian block diagonalizes into four 2×2 matrices, each of which has the form of a spinless $p \pm ip$ superconductor. Gaps close at Γ for $\pm\lambda \pm \Delta = m_0$. For $|\lambda| > m_0$, *i.e.* when the QAH effect occurs, weak pairing gives rise to superconducting states with Chern numbers ± 2 , corresponding to Nambu-doubled quantum Hall edge states. As explained below, we propose using these states as a resource for MZM formation. (The Chern number phase diagram of our proximitized MTI model is described in detail in the Supplementary Material.)

Our main interest is in the possibility of gate-defined quasi-1D topological regions embedded within the 2D film surface. To set the stage, however, we first address the closely related case of narrow ribbons [10, 31, 32]. For width $W = 1$, where W is the number of lattice model rows, the $\Delta_t = -\Delta_b$ BdG Hamiltonian reduces to four effective Kitaev chains. The Supplementary Material contains a detailed summary of how the Z_2 (1D) topological phase diagram of the $\Delta_t = -\Delta_b$ model depends on W . In Fig. 2 we plot the Z_2 phase diagram in (λ, μ) space for a ribbon with proximity coupling only to the bottom MTI surface. The Z_2 invariant is evaluated using $\nu = \text{sgn}[\text{Pf}\tilde{H}(0)]\text{sgn}[\text{Pf}\tilde{H}(\pi)]$, where \tilde{H} is the skew-symmetrized Hamiltonian obtained by switching H_{BdG} to the Majorana basis, Pf denotes the Pfaffian number and $\text{sgn}[x]$ is the sign of x . More information about the

calculation of Z_2 invariant is shown in the Supplementary Material. For weak pairing $\nu = \pm 1$ depending on whether the number of normal state bands that cross the Fermi level is even or odd.

The broad region of topologically nontrivial behavior at large λ and small μ in Fig. 2, *i.e.* when the unproximitized MTI is in a QAH state, reflects the property that only a single ribbon band is present in this energy range at any value of W . The Z_2 invariant is qualitatively more sensitive to λ , μ , W and other ribbon model parameters at larger values of μ that lie within the gapped surface state bands. For a lattice model of a normal 2D p-wave superconductor, for example, there are $4W$ phase boundaries in the quasi-1D Z_2 classification of ribbon states at width W . This sensitivity is not favorable for reliable realization of either trivial or non-trivial states. In the QAH state there is at most a single band, but the MZMs present for finite ribbon length are protected only by exponentially small superconducting gaps ($\sim \Delta e^{-W/\xi}$), where $\xi \sim v/(\lambda - m_0)$ is the 2D edge state localization length in lattice constant units, making the Z_2 classification academic. (For typical parameters $\xi \sim 10\text{nm}$) In order to obtain MZMs that are reasonably localized near ribbon edges it is necessary to have ribbon widths that are not too large compared to ξ , and also to be able to conveniently tune between topologically trivial and non-trivial states. Since the exchange coupling parameter λ in Fig. 2 is fixed for a given MTI sample and a given operating temperature, a different tuning parameter must be identified.

Quantum Anomalous Hall Ribbon Majoranas: We propose controlling MZMs in ribbons by placing a MTI film that supports a QAH state on a superconducting substrate and fabricating a top gate. Varying the gate field will alter the carrier density (and hence the chemical potential μ) of the MTI, and also shift the energy of the top surface Dirac cone relative to the bottom surface. The latter effect is due to the unscreened portion of the gate electric field that survives in the interior of the TI and is represented in our model by the parameter λ' . Applying a gate voltage moves the system along a line in (μ, λ') space that depends on the effective bulk dielectric constant of the TI. As we now show a gate voltage can therefore tune the proximitized MTI between $Z_2 = 0$ and $Z_2 = 1$ ribbon states.

Fig. 3 illustrates 2D Chern number phase diagrams in (λ', μ) space for MTIs on superconducting substrates with $\Delta_b = 0.2m_0$ and $\Delta_t = 0$, at three different values of exchange field λ . For $\lambda < m_0$ (left panel), the unproximitized MTI is in a normal insulator state, but superconductivity that is sufficiently strong can still induce odd Chern number BdG states. Our main interest is in the case in the right panel where $\lambda > m_0$ so that the unproximitized MTI is in a QAH state at $\lambda' = 0$. Proximitized superconductivity of QAH states is now routinely achieved experimentally [25, 26]. The QAH state occurs

at small $|\mu|$ only when $\sqrt{\lambda'^2 + m_0^2} < |\lambda|$; the gate field λ' efficiently converts a QAH insulator with edge states into a normal insulator with no edge states in the gap, and no opportunity for Z_2 states in ribbons.

For weak pairing, ribbons have $Z_2 = 1$ states when an odd number of subbands cross the Fermi level. In a ribbon formed from a semiconductor quantum well with strong Zeeman and spin-orbit coupling, or from an MTI with $\lambda \ll m_0$, a series of closely spaced non-degenerate 1D sub-bands appear close to the extrema of the bulk 2D bands, as illustrated schematically in Fig. 4a. When the ribbon width increases, the spacing between subbands becomes smaller and the Z_2 phase diagrams will have more closely spaced boundaries between $Z_2 = 0$ and $Z_2 = 1$ phases. In the $\lambda \gg m_0$ QAH case on the other hand, illustrated schematically in Fig. 4b, a single pair of bands crosses the Fermi level at all energies inside the bulk 2D gap, except for a narrow gapped region due to the avoided crossing between QAH edge states localized on opposite sides of the ribbon. The system is therefore almost always nontrivial in the broad range $\mu \in (-E_b, E_b)$, where E_b is the bulk gap, independent of the ribbon width.

In Fig. 4c we plot the Z_2 phase diagram in (μ, λ') plane of $W = 300$, $m_0 = 6\text{meV}$, $m_1 = 0.2\text{eV}$, $v = 0.7\text{eV}$, $\lambda = 12\text{meV}$, $\Delta_b = 1\text{meV}$, $\Delta_t = 0$ ribbon, which exhibits large adjacent trivial and nontrivial regions near $\mu = 0$. For these realistic parameters $|\lambda|$ is larger than m_0 , but not much larger. (Larger QAH regions can be achieved by going to thicker films with smaller m_0 but only at the expense of reducing all relevant energy scales.) QAH edge states overlap strongly even at $W = 300$, so strongly in fact that the normal state gap produced by avoided crossing of edge states is comparable to m_0 , creating a substantial $Z_2 = 0$ region near $\mu = 0$. This region is however still bordered at $\lambda' = 0$ by a large $Z_2 = 1$ region that can be identified with pairing of QAH edge states. The gate field λ' sweeps this state into a large adjacent $Z_2 = 0$ region, which can be identified with a proximity coupled ordinary insulator.

Fig. 4d plots the ribbon width dependence of the gap at $k_x = 0$, $\lambda' = 0$, and $\mu = 5\text{meV}$ out to $W \sim 1000$ in lattice constant units. Here we notice that there is only one gap closing as a function of W which signals a phase transition between a small W $Z_2 = 0$ state associated with a large avoided crossing gap between QAH edge states, and a large W $Z_2 = 1$ state associated with pairing of QAH edge states. The gaps remain large out to ~ 1000 lattice constants, corresponding to a physical length $\sim 400\text{nm}$, partly because the edge state localization length is enhanced by the relatively high velocity of quantum Hall edge states compared to the velocity of states present near the bottom of a bulk 2D band. As the system becomes wider, the QAH edge states have less overlap and the gap is eventually reduced to very small values.

Because of the bulk-edge correspondence of topologi-

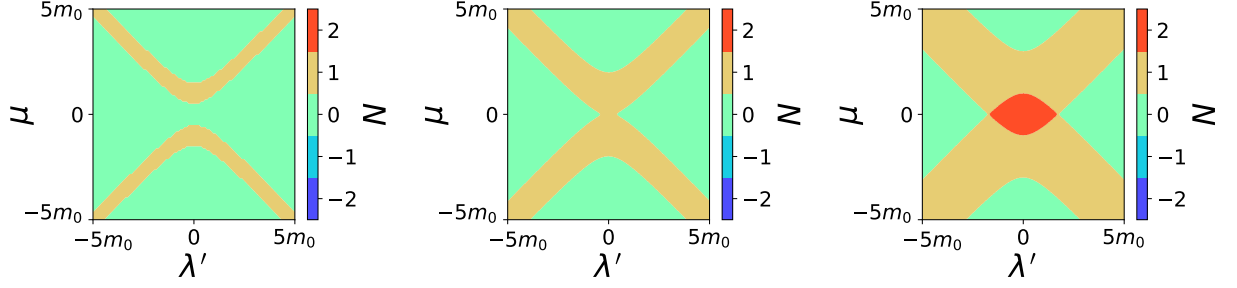


FIG. 3: Phase diagram of a MTI on a superconducting substrate in λ' - μ space. Here $\Delta_b = 0.2m_0$, $\Delta_t = 0$, and from left to right $\lambda = 0.5m_0$, m_0 , and $2m_0$.

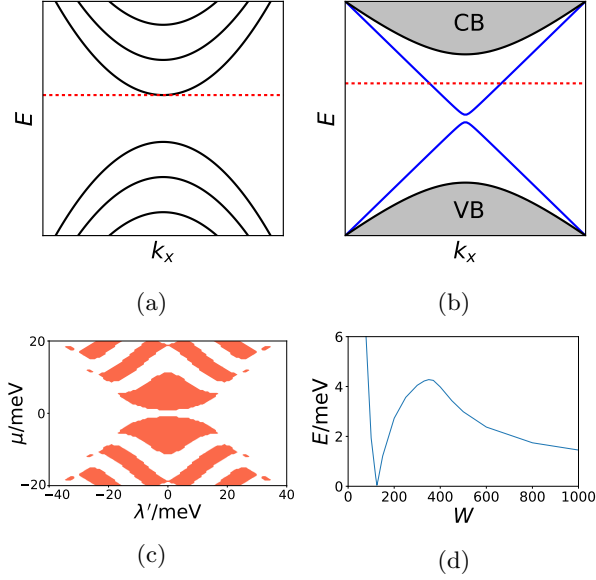


FIG. 4: (a) Bandstructure of a nanoribbon. When the Fermi level (the red dotted line) coincides with the bottom of a subband, a TPT occurs; (b) Bandstructure in the QAH regime. Grey regions are conduction and valence bands, blue curves are edge states with a small hybridization gap, and the red dotted line shows the Fermi level. When the chemical potential is inside the bulk gap and outside the hybridization gap, with SC the system should always be nontrivial. (c) Phase diagram in λ' - μ space for a quasi-1D chain with $W = 300$, $m_0 = 6$ meV, $m_1 = 0.2$ eV, $v = 0.7$ eV, $\lambda = 12$ meV, $\Delta_b = 1$ meV, $\Delta_t = 0$; (d) Relation between gap and width, with $\mu = 5$ meV, $\lambda' = 0$ and other parameters the same as in (c).

cal states we expect Majorana zero modes to appear not only in ribbons, but also in wide films in which quasi-one-dimensional regions are formed that have local model parameters in the topologically non-trivial range. In order to define a quasi-1D region, we can form a gate array above a proximitized MTI thin film whose chemical po-

tential is in the QAH gap, as illustrated schematically in Fig. 1. Just as in the ribbon case, the gate electric field λ' will form local regions that have $Z_2 = 0$ and Chern number $N = 0$, isolating the $Z_2 = 1$ and $N = 1$ or 2 regions along the less strongly disturbed portions of the MTI thin film. As discussed in the Supplementary Material, we have explicitly verified that MZMs appear near the ends of quasi-1D topological superconductors that are written onto the MTI surface in this way.

Conclusion: Topological quantum computation requires flexible Majorana braiding that relies on branched structures like T-junctions [27]. Although conceptually simple, T-junctions based on semiconductor quantum wires are difficult to build because of challenges in depositing aligned semiconductor quantum wires. We have demonstrated the possibility of using gate arrays to write MZMs onto the surface of a 2D MTI placed on a superconducting substrate. It has some similarities with systems [33, 34] in which a gate array writes quantum wires onto a quantum well by periodically depleting all carriers, or varying the number of locally occupied subbands between even and odd values, but has advantages in this case as well because *i*: it is not necessary to apply a magnetic field to break degeneracies at time-reversal invariant points in one-dimensional momentum space and because *ii*: there can be a large energy separation between the quasi-1D bands formed by quantum Hall edge states and higher energy subbands, providing a large target for efforts to tune to $Z_2 = 1$ superconductors. Additionally, our proposal also provides an ideal platform for building the Majorana box qubits recently proposed in Refs. 7 and 28 because *i*: it is easy to define arbitrary number of parallel gate-controlled quasi-1D TSC wires as shown in Fig. 1a, and *ii*: because large topological stability ranges allows geometrical capacitance[7] to be changed without changing topological states.

This work was supported by the Army Research Office (ARO) under contract W911NF-15-1-0561:P00001, and by the Welch Foundation under grant TBF1473.

**SUPPLEMENTARY MATERIAL FOR
A QUANTUM ANOMALOUS HALL MAJORANA PLATFORM**

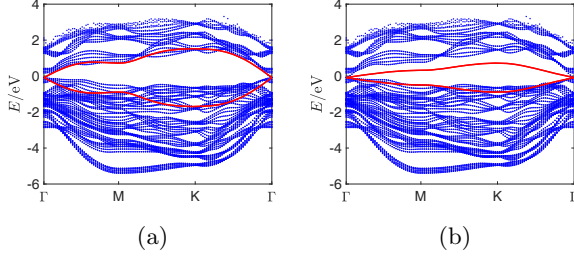


FIG. 5: Bandstructure of a 5-layer Bi_2Se_3 thin film. Blue dots are from DFT calculation, while red curves are from our effective lattice model when we choose $m_0 = 6 \text{ meV}$ and (a) $m_1 = 0.2 \text{ eV}$, $v = 0.7 \text{ eV}$; (b) $m_1 = 0.1 \text{ eV}$, $v = 0.2 \text{ eV}$.

MATERIAL PARAMETERS

Density functional theory performed with Vienna Ab initio simulation package (VASP) is used to calculate the electronic structure of 5-layer Bi_2Se_3 , and the bandstructure is shown in Fig. 5. The bandstructure from the lattice model is also plotted, with a rough estimate of the hybridization of two surfaces $m_0 = 6 \text{ meV}$, $m_1 = 0.2 \text{ eV}$ and Fermi velocity $v = 0.7 \text{ eV}$ in Fig. 5a, and $m_0 = 6 \text{ meV}$, $m_1 = 0.1 \text{ eV}$, $v = 0.2 \text{ eV}$ in Fig. 5b, which are two limits with the parameters fitting well with the surface band above and below the Fermi level). The lattice model has good agreement with DFT results and experiments.

LATTICE MODEL

With substitutions $k_{x/y} \rightarrow \sin k_{x/y}$ and $k^2 \rightarrow 2(2 - \cos k_x - \cos k_y)$, we can rewrite the momentum-space Hamiltonian in the following form

$$H_0(\mathbf{k}) = h_0 + (h_x e^{ik_x} + h_y e^{ik_y} + h.c.) \quad (5)$$

Then we obtain a nearest-neighbor tight-binding model, where the onsite term is

$$h_0 = (m_0 + 4m_1)\tau_x + \lambda\sigma_z + \lambda'\tau_z \quad (6)$$

and the hopping terms in x and y directions are

$$h_x = -\frac{i}{2}v\sigma_x - m_1\tau_x \quad (7)$$

$$h_y = \frac{i}{2}v\sigma_y - m_1\tau_x \quad (8)$$

With s -wave SC, the on-site and hopping matrices become

$$h_0^{\text{sc}} = \begin{pmatrix} h_0 - \mu & \Delta_{\text{sc}} \\ \Delta_{\text{sc}}^\dagger & -h_0^* + \mu \end{pmatrix} \quad (9)$$

$$h_x^{\text{sc}} = \begin{pmatrix} h_x & 0 \\ 0 & -h_x^* \end{pmatrix} \quad (10)$$

$$h_y^{\text{sc}} = \begin{pmatrix} h_y & 0 \\ 0 & -h_y^* \end{pmatrix} \quad (11)$$

BLOCK DIAGONALIZATION OF THE BDG MATRIX

In the new basis $\phi_{\mathbf{k}} = U\psi_{\mathbf{k}}$, where

$$U = \frac{1}{2} \begin{pmatrix} 1 & 0 & 1 & 0 & 0 & 1 & 0 & -1 \\ 0 & 1 & 0 & -1 & 1 & 0 & 1 & 0 \\ 0 & -1 & 0 & 1 & 1 & 0 & 1 & 0 \\ 1 & 0 & 1 & 0 & 0 & -1 & 0 & 1 \\ 0 & 1 & 0 & 1 & 1 & 0 & -1 & 0 \\ 1 & 0 & -1 & 0 & 0 & 1 & 0 & 1 \\ -1 & 0 & 1 & 0 & 0 & 1 & 0 & 1 \\ 0 & 1 & 0 & 1 & -1 & 0 & 1 & 0 \end{pmatrix} \quad (12)$$

the BdG matrix can be block-diagonalized

$$H_{\text{BdG}}(\mathbf{k}) = \text{diag}\{\mathbf{d}_1 \cdot \boldsymbol{\sigma}, \mathbf{d}_2 \cdot \boldsymbol{\sigma}, \mathbf{d}_3 \cdot \boldsymbol{\sigma}, \mathbf{d}_4 \cdot \boldsymbol{\sigma}\} \quad (13)$$

where

$$\begin{aligned} \mathbf{d}_1 &= (v \sin k_y, -v \sin k_x, m_0 + \lambda + \Delta \\ &\quad + 2m_1(2 - \cos k_x - \cos k_y)) \\ \mathbf{d}_2 &= (-v \sin k_y, -v \sin k_x, -m_0 - \lambda + \Delta \\ &\quad - 2m_1(2 - \cos k_x - \cos k_y)) \\ \mathbf{d}_3 &= (v \sin k_y, v \sin k_x, m_0 - \lambda - \Delta \\ &\quad + 2m_1(2 - \cos k_x - \cos k_y)) \\ \mathbf{d}_4 &= (-v \sin k_y, v \sin k_x, -m_0 + \lambda - \Delta \\ &\quad - 2m_1(2 - \cos k_x - \cos k_y)) \end{aligned} \quad (14)$$

For each block the Chern number can be calculated with the formula

$$N_i = \frac{1}{4\pi} \int_{\text{BZ}} d^2k \hat{\mathbf{d}}_i \cdot (\partial_{k_x} \hat{\mathbf{d}}_i \times \partial_{k_y} \hat{\mathbf{d}}_i) \quad (15)$$

Then the Chern number of the whole system is $N = \sum_{i=1}^4 N_i$. The phase diagram is shown in Fig. 6a.

A general $p \pm ip$ TSC in 2D is described by Hamiltonian $H_p = \mathbf{h} \cdot \boldsymbol{\sigma}$, with $\mathbf{h} = (\Delta_p \sin k_x, \pm \Delta_p \sin k_y, 2t(2 - \cos k_x - \cos k_y) - \mu)$. In its non-trivial phase $|\mu| < 2t$ the

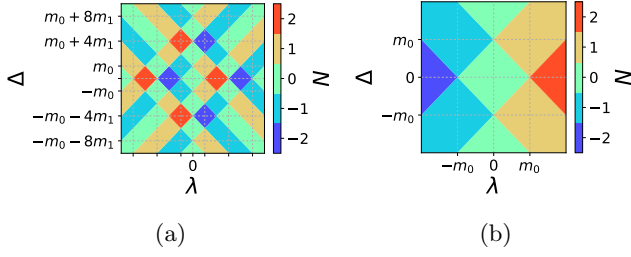


FIG. 6: Lattice (a) and continuum (b) model Chern number N phase diagrams for 2D geometries with $\lambda' = \mu = 0$ and $\Delta_t = -\Delta_b = \Delta$. For visualization purposes (a) is plotted at an unphysically small value of m_1/m_0 .

chiral Majorana mode appear, which is localized in the $\xi_P \sim \frac{\Delta}{|\mu|}$ width near the edge. Comparing \mathbf{h} with \mathbf{d}_i s, we get edge mode localization lengths for effective $p \pm ip$ superconductors of (13).

$$\begin{aligned} \xi_1 &= \frac{v}{|m_0 + \lambda + \Delta|} & \xi_2 &= \frac{v}{|-m_0 - \lambda + \Delta|} \\ \xi_3 &= \frac{v}{|m_0 - \lambda - \Delta|} & \xi_4 &= \frac{v}{|-m_0 + \lambda - \Delta|} \end{aligned} \quad (16)$$

For a 1D wire, y -direction hopping is ignored, so the effective Hamiltonian for 3DTI surface states becomes $h_{\text{eff}}(k_x) = -\sin k_x \sigma_y$, and the hybridization term becomes $m_k = m_0 + 2m_1(1 - \cos k_x)$. If we still assume $\lambda' = \mu = 0, \Delta_t = -\Delta_b = \Delta$, then when we perform the same basis transformation as above, the BdG matrix will be block-diagonalized into four 2×2 blocks. If we consider the first block, which is (we write k_x as k for simplicity)

$$h_1(k) = \begin{pmatrix} m_k + \lambda + \Delta & iv \sin k \\ -iv \sin k & -m_k - \lambda - \Delta \end{pmatrix} \quad (17)$$

with the basis $(\alpha_k, \alpha_{-k}^\dagger)^T$ where $\alpha_k = c_{k\uparrow}^\dagger + c_{k\uparrow}^\dagger + c_{-k\downarrow}^\dagger - c_{-k\downarrow}^\dagger$. For a wire with N lattice sites, the Hamiltonian can be written in real space:

$$\begin{aligned} h_1 &= (m_0 + 2m_1 + \lambda + \Delta) \sum_{j=1}^N \alpha_j^\dagger \alpha_j \\ &+ \sum_{j=1}^{N-1} (m_1 \alpha_j^\dagger \alpha_{j+1} - \frac{v}{2} \alpha_j \alpha_{j+1} + h.c.) \end{aligned} \quad (18)$$

This is in the same form as a Kitaev chain [10]. When $|m_0 + 2m_1 + \lambda + \Delta| < 2m_1$, Majorana fermions will appear at the ends. When we consider all the four blocks, the resulting phase diagram is shown in Fig. 7a.

For a quasi-1D system with larger width W , the Hamiltonian is an $8W \times 8W$ matrix. It can still be diagonalized into four blocks, each of size $2W \times 2W$. The phase boundaries cannot be solved analytically, but we can prove that

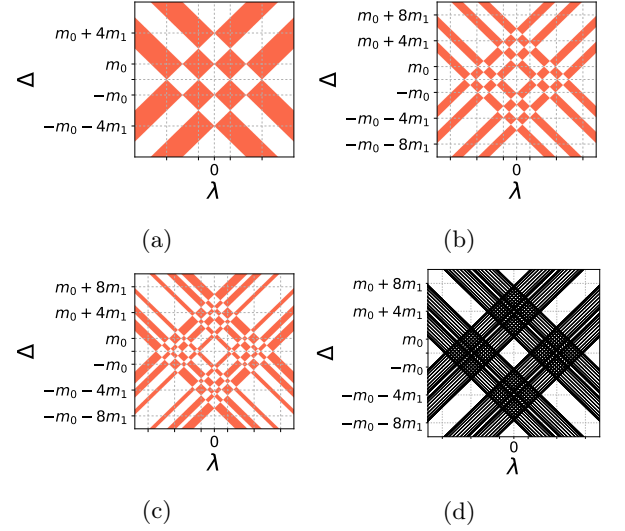


FIG. 7: Phase diagrams of (quasi-)1D systems with $\lambda' = \mu = 0, \Delta_t = -\Delta_b = \Delta$, and chain width $W =$ (a)1 (b)2 (c)3 (d)10. In (a)(b)(c), red and white regions are respectively topologically nontrivial and trivial. The phase diagram will vary continuously as $\Delta_{t,b}$ and other model parameters are varied. Only the phase boundaries are plotted in (d). For visualization purposes these figures are plotted for an unphysically small value of m_1/m_0 .

they are still straight lines. For $W = 1, 2, 3$ and 10, the phase diagrams are shown in Fig. 7. When W increases, more phase boundaries appear, resulting in an alternating pattern in the phase diagrams. When W is large enough, the outline of the pattern will look very similar to that in Fig. 6a.

Z_2 INVARIANT

The Z_2 invariant of a 1D system can be obtained by Pfaffian calculation. For a BdG matrix in the form

$$H_{\text{BdG}}(k) = \begin{pmatrix} h(k) & \Delta \\ \Delta^\dagger & -h^*(-k) \end{pmatrix} \quad (19)$$

where $h(k)$ and Δ are matrices, a skew-symmetrized matrix can be obtained in Majorana basis:

$$\begin{pmatrix} \gamma_1 \\ \gamma_2 \end{pmatrix} = \frac{1}{\sqrt{2}} \begin{pmatrix} 1 & 1 \\ -i & i \end{pmatrix} \begin{pmatrix} c^\dagger \\ c \end{pmatrix} \quad (20)$$

with γ_i is the creation operator of Majorana Fermion and c^\dagger/c is the creation/annihilation operator of electrons. Then we can get the skew-symmetrized Hamiltonian as:

$$\tilde{H}(k) = U H_{\text{BdG}}(k) U^\dagger \quad (21)$$

where

$$U = \frac{1}{\sqrt{2}} \begin{pmatrix} 1 & 1 \\ -i & i \end{pmatrix} \quad (22)$$

where the numbers denote matrices proportional to the identity matrix with the same dimension as $h(k)$. Then

$$\tilde{H}(k) = \begin{pmatrix} h(k) - h^*(-k) + \Delta + \Delta^\dagger & i(h(k) + h^*(-k) - \Delta + \Delta^\dagger) \\ -i(h(k) + h^*(-k) + \Delta - \Delta^\dagger) & h(k) - h^*(-k) - \Delta - \Delta^\dagger \end{pmatrix} \quad (23)$$

Since $h(k) = h(-k) = h^\dagger(-k)$, $\Delta^\dagger = -\Delta^*$, $\tilde{H}(k)$ is a skew-symmetric matrix. The Z_2 invariant can then be evaluated as $\nu = \text{sgn}[\text{Pf}\tilde{H}(0)]\text{sgn}[\text{Pf}\tilde{H}(\pi)]$, where Pf denotes the Pfaffian number and $\text{sgn}[x]$ is the sign of x . Numerical calculation of the Pfaffian number is performed using the Pfpack code [35].

FITTING THE LOWER BAND

In the main text, all calculations are based on parameters from Fig. 5a, which fit the upper band pretty well. Here we present results from calculations with much smaller v and m_1 ($v = 0.2 \text{ meV}$, $m_1 = 0.1 \text{ meV}$), which give better fitting of the surface band below the Fermi level as shown in Fig. 5b.

Fig. 8 shows results from calculation with lower-band parameters. The phase diagrams show more narrow alternating patterns, but near $\mu = 0$ large topological regions still exist. Large v, m_1 and small Δ ensures a large gap protecting MZMs. Therefore, as long as $v, m_1 \gg m_0, \Delta$, our results in the main text always hold true, and the proposed experimental scheme is always feasible.

SPATIAL DISTRIBUTION

Now we construct a finite system and calculate the spatial distribution of MZM. A topological quasi-1D region is embedded in the system, surrounded by regions with large λ' . For numerical convenience, here we choose some fictitious parameters with small v and m_1 , instead of more realistic ones. The result is shown in Fig. 9. The numerical calculation was performed using the Kwant code [36].

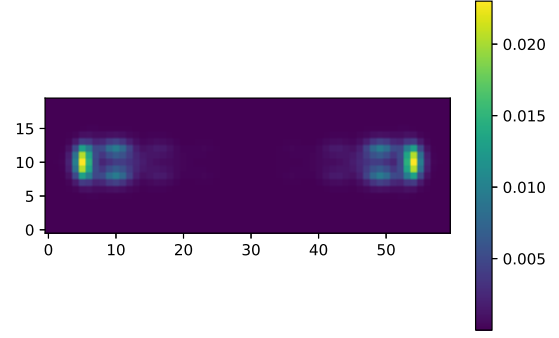


FIG. 9: Spatial distribution of the lowest energy eigenstate, where a 50×5 quasi-1D region is embedded in a 60×20 system, and $m_0 = 1, m_1 = 2, v = 2, \lambda = 2, \mu = 1, \Delta_t = 1, \Delta_b = 0$. Inside and outside the quasi-1D region, $\lambda' = 0$ and 4 respectively.

-
- [1] D. A. Ivanov, Physical Review Letters **86**, 268 (2001), pRL.
 - [2] C. Nayak, S. H. Simon, A. Stern, M. Freedman, and S. Das Sarma, Reviews of Modern Physics **80**, 1083 (2008), rMP.
 - [3] A. Y. Kitaev, Annals of Physics **303**, 2 (2003).
 - [4] A. Kitaev, Annals of Physics **321**, 2 (2006).
 - [5] S. D. Sarma, M. Freedman, and C. Nayak, **1**, 15001 (2015).
 - [6] D. Aasen, M. Hell, R. V. Mishmash, A. Higginbotham, J. Danon, M. Leijnse, T. S. Jespersen, J. A. Folk, C. M. Marcus, K. Flensberg, and J. Alicea, Physical Review X **6**, 031016 (2016), pRX.
 - [7] T. Karzig, C. Knapp, R. M. Lutchyn, P. Bonderson, M. B. Hastings, C. Nayak, J. Alicea, K. Flensberg, S. Plugge, Y. Oreg, C. M. Marcus, and M. H. Freedman, Physical Review B **95**, 235305 (2017), pRB.
 - [8] G. Moore and N. Read, Nuclear Physics B **360**, 362 (1991).
 - [9] H.-H. Sun and J.-F. Jia, npj Quantum Materials **2**, 34 (2017).
 - [10] A. Y. Kitaev, Physics-Uspekhi **44**, 131 (2001).
 - [11] A. Jason, Reports on Progress in Physics **75**, 076501 (2012).
 - [12] R. M. Lutchyn, J. D. Sau, and S. Das Sarma, Physical Review Letters **105**, 077001 (2010), pRL.
 - [13] J. D. Sau, R. M. Lutchyn, S. Tewari, and S. Das Sarma, Physical Review Letters **104**, 040502 (2010), pRL.
 - [14] C. Beenakker, Annual Review of Condensed Matter Physics **4**, 113 (2013).
 - [15] L. Fu and C. L. Kane, Physical Review Letters **100**, 096407 (2008), pRL.
 - [16] V. Mourik, K. Zuo, S. M. Frolov, S. R. Plissard, E. P. A. M. Bakkers, and L. P. Kouwenhoven, Science **336**, 1003 (2012).

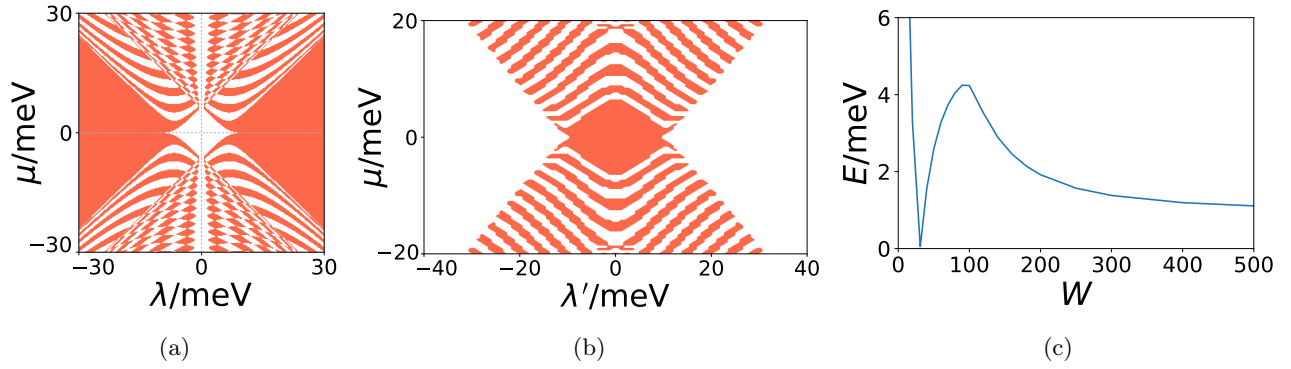


FIG. 8: (a) Phase diagram in λ - μ space for a quasi-1D chain with $W = 300$, $m_0 = 6$ meV, $m_1 = 0.1$ eV, $v = 0.2$ eV, $\lambda' = 0$, $\Delta_b = 1$ meV, $\Delta_t = 0$; (b) Phase diagram in λ' - μ space with $\lambda = 12$ meV and other parameters the same as in (a); (c) Relation between gap and width, with $\mu = 5$ meV, $\lambda = 12$ meV and other parameters the same as in (a).

- [17] M. T. Deng, C. L. Yu, G. Y. Huang, M. Larsson, P. Caroff, and H. Q. Xu, *Nano Letters* **12**, 6414 (2012).
- [18] A. Das, Y. Ronen, Y. Most, Y. Oreg, M. Heiblum, and H. Shtrikman, *Nat Phys* **8**, 887 (2012), 10.1038/nphys2479.
- [19] M. T. Deng, S. Vaitieknas, E. B. Hansen, J. Danon, M. Leijnse, K. Flensberg, J. Nygrd, P. Krogstrup, and C. M. Marcus, *Science* **354**, 1557 (2016).
- [20] L. P. Rokhinson, X. Liu, and J. K. Furdyna, *Nat Phys* **8**, 795 (2012), 10.1038/nphys2429.
- [21] S. M. Albrecht, A. P. Higginbotham, M. Madsen, F. Kuemmeth, T. S. Jespersen, J. Nygrd, P. Krogstrup, and C. M. Marcus, *Nature* **531**, 206 (2016).
- [22] S. Nadj-Perge, I. K. Drozdov, J. Li, H. Chen, S. Jeon, J. Seo, A. H. MacDonald, B. A. Bernevig, and A. Yazdani, *Science* **346**, 602 (2014).
- [23] R. Pawlak, M. Kisiel, J. Klinovaja, T. Meier, S. Kawai, T. Glatzel, D. Loss, and E. Meyer, *NPJ Quantum Information* **2**, 16035 (2016).
- [24] R. Yu, W. Zhang, H.-J. Zhang, S.-C. Zhang, X. Dai, and Z. Fang, *Science* **329**, 61 (2010).
- [25] C.-Z. Chang, J. Zhang, X. Feng, J. Shen, Z. Zhang, M. Guo, K. Li, Y. Ou, P. Wei, L.-L. Wang, Z.-Q. Ji, Y. Feng, S. Ji, X. Chen, J. Jia, X. Dai, Z. Fang, S.-C. Zhang, K. He, Y. Wang, L. Lu, X.-C. Ma, and Q.-K. Xue, *Science* **340**, 167 (2013).
- [26] Q. L. He, L. Pan, A. L. Stern, E. C. Burks, X. Che, G. Yin, J. Wang, B. Lian, Q. Zhou, E. S. Choi, K. Murata, X. Kou, Z. Chen, T. Nie, Q. Shao, Y. Fan, S.-C. Zhang, K. Liu, J. Xia, and K. L. Wang, *Science* **357**, 294 (2017).
- [27] J. Alicea, Y. Oreg, G. Refael, F. von Oppen, and M. P. A. Fisher, *Nat Phys* **7**, 412 (2011), 10.1038/nphys1915.
- [28] S. Plugge, A. Rasmussen, R. Egger, and K. Flensberg, *New Journal of Physics* **19**, 012001 (2017).
- [29] D. J. J. Marchand and M. Franz, *Physical Review B* **86**, 155146 (2012), pRB.
- [30] J. Wang, Q. Zhou, B. Lian, and S.-C. Zhang, *Physical Review B* **92**, 064520 (2015).
- [31] A. C. Potter and P. A. Lee, *Physical Review Letters* **105**, 227003 (2010), pRL.
- [32] S. Tewari and J. D. Sau, *Physical Review Letters* **109**, 150408 (2012), pRL.
- [33] F. Pientka, A. Keselman, E. Berg, A. Yacoby, A. Stern, and B. I. Halperin, *Physical Review X* **7**, 021032 (2017), pRX.
- [34] M. Hell, M. Leijnse, and K. Flensberg, *Phys. Rev. Lett.* **118**, 107701 (2017).
- [35] M. Wimmer, *ACM Transactions on Mathematical Software (TOMS)* **38**, 30 (2012).
- [36] C. W. Groth, M. Wimmer, A. R. Akhmerov, and X. Waintal, *New Journal of Physics* **16**, 063065 (2014).